# Sparse Imaging for Spinning Space Targets with Short Time Observation

Le Kang[1], Bi-shuai Liang[1], Ying Luo[*] and Qun Zhang

Abstract—**Inverse synthetic aperture radar (ISAR) imaging is an important technique for moving target identification and classification. For the space spinning targets, a long-time observation is required to estimate the spinning parameter in the conventional ISAR imaging methods. However, for the advanced multifunctional radar, which is used for multi-target surveillance, a long-time observation for only one target is the loss outweighs the gain. To decrease the observation time, we propose a novel imaging method for spinning space targets with short time observation in this paper. Firstly, we build the imaging model by using the azimuth rotation angle caused by the spinning motion rather than the translation motion to obtain the azimuth resolution. Secondly, we utilize the orthogonal coding signals with different delays to obtain enough equivalent pulses in the short observation time. Moreover, since the equivalent pulses are block-missing to avoid overlapping of the transmitting duration and the receiving duration, we transform the imaging problem to the compressed sensing (CS) problem and solve it by modifying the Smoothed L0-norm (SL0) algorithm. Finally, both the simulations and the experiments on real data are shown to demonstrate the validity of the proposed method. Since the observing time of the proposed method only needs to cover a small percentage of one spinning period, the proposed method can be used in multi-target surveillance such as satellites and space debris.**

Index Terms—**Radar imaging, spinning space target, orthogonal coding signal, compressed sensing.**
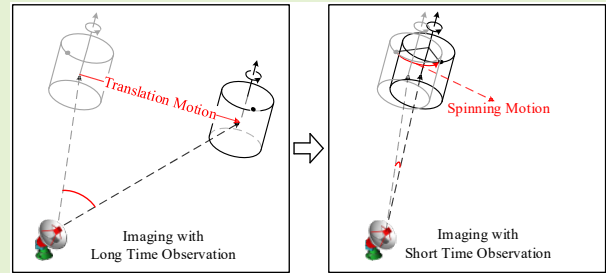
I. INTRODUCTION

RECENTLY, due to the developments in the utilization of space resources, the number of space debris has risen rapidly [1]. Therefore, the detection, identification, and classification of space debris have attracted more attention. Optical communication systems have many advantages, but optical remote sensor for space debris is easy to be affected by the observation conditions [2-4]. Thanks to the advantages of all-weather, all-day, and long-distance, inverse synthetic aperture radar (ISAR) is widely adopted to obtain space debris images [5-7]. It obtains the range-resolution by transmitting the wideband signal, and the azimuth resolution by azimuth rotation angle caused by the relative motion between the sensors and the objectives. After the accurate translation compensation, the ISAR imaging geometry is the turntable model, and the well-focused radar images can be generated by the classical imaging methods, e.g., Range-Doppler (RD) method [8] and the sparse imaging method [9-11].

For spinning space targets, however, the additional time-varying, periodical Doppler frequency modulations on radar echoes are induced by the spinning motion, which is a kind of micro-Doppler phenomenon [12-13]. In wide-band radar imaging, the micro-Doppler phenomenon appears as the m-D curve reflecting range cell migration (RCM) in the range-slow-time domain. Generally, the slowly varying RCM can be corrected by phase compensation by utilizing the high-order phase to approximate the phase caused by spinning motion [14-15]. Since both the order of the compensated phase and the approximation error increase with the spinning velocity, the imaging performance of this method is unacceptable for rapidly spinning targets. To solve this problem, the Hough transform [16] and the inverse Radon transform [17] are utilized to estimate the spinning parameters, and the empirical mode decomposition (EMD) [18] is introduced to separate the micro-motion component. Moreover, the spinning parameter estimation and 3D imaging methods based on range instantaneous doppler (RID) are proposed for spinning space targets [19-20]. Since the spinning parameter estimation is the core issue of the above imaging methods, these methods require the observation for several spinning periods. The observation requirement is acceptable for single-target surveillance. However, for multi-target surveillance, a long-time observation for only one target is the loss outweighs the gain. Therefore, the imaging method for spinning space targets with short time observation is desired.

What the abovementioned methods have in common is that the azimuth resolution is determined by the azimuth rotation

1 These authors contributed equally to this work.
* Corresponding author. e-mail: luoying2002521@163.com;
L. Kang, B. S. Liang, Y. Luo, and Q. Zhang are with the Institute of Information and Navigation, Air Force Engineering University, Xi'an 710077, P. R. China, and with the Collaborative Innovation Center of Information Sensing and Understanding, Xi'an, 710077, P. R. China.
Y. Luo and Q. Zhang are also with the Key Laboratory for Information Science of Electromagnetic Waves (Ministry of Education), Fudan University, Shanghai 200433, P. R. China.
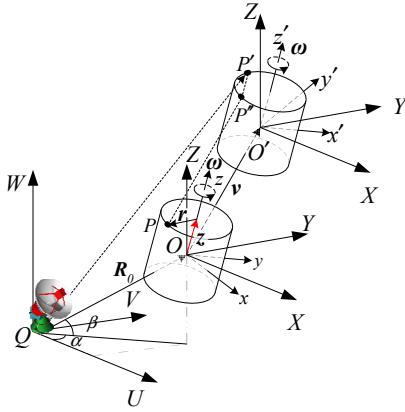
Fig. 1. The geometry of the spinning space target.

angle, which is caused by the target motion in addition to the spinning motion. However, the spinning motion of targets can also produce the azimuth rotation angle between the scatterers and the radar. There are two advantages to achieve an azimuth rotation angle by the spinning motion rather than the translation motion. Firstly, the observation time will be significantly reduced since only a small percentage of one spinning period needs to be covered. Secondly, the RCM in the range-slow-time domain is slight during a short-time observation.

In this paper, we propose a novel sparse imaging method for spinning space targets with short time observation. We utilize the azimuth rotation angle caused by the target spinning to obtain the azimuth resolution. To obtain enough azimuth sampling points in the short observation time, we utilize the multiple Gold coding sequences [21] with different delays to achieve high virtual pulse repetition frequency (PRF). Since the virtual pulses are block-missed to avoid overlapping of the transmitting duration and the receiving duration, the azimuth compression can be solved by modifying the Smoothed L0-norm (SL0) algorithm [22]. Finally, the experiments on real data demonstrate that the observing time of the proposed method only needs to cover a small percentage of one spinning period, and the large RCM in the range-slow-time domain is avoided.

II. SPINNING SPACE TARGET IMAGING MODEL BASED ON ORTHOGONAL CODED SIGNAL

A. Geometry of the spinning space target

The geometry of the radar and the spinning space target is shown in Fig. 1, in which the point Q is the original point of the global coordinate system (U,V,W). The reference coordinate system (X,Y,Z) translating with the target is parallel to the global coordinate system (U,V,W). At the initial moment, the vector from the target center O and the radar Q is $\boldsymbol{R}_0$. (x,y,z) with the original point O is the target local coordinate system. The translation velocity to the global coordinate system is $\boldsymbol{v}$. The target is rotating around the z-axis with the velocity $\boldsymbol{\omega}=(0,0,\omega_z)^{\mathrm{T}}$ in the local coordinate system. Suppose the target is rotating spinning with the velocity $\hat{\boldsymbol{\omega}}=(\omega_X,\omega_Y,\omega_Z)^{\mathrm{T}}$

in the reference coordinate system, $\hat{\boldsymbol{\omega}}=\mathscr{R}_{\text{init}}\boldsymbol{\omega}$ holds and $\mathscr{R}_{\text{init}}$ is the Euler rotation matrix.

For any scatterer P on the target, $\overrightarrow{OP}$ in the local coordinate system is $\boldsymbol{r}_0=(r_{x0},r_{y0},z_0)^{\mathrm{T}}$ at the initial moment. Then $\boldsymbol{r}_0=\boldsymbol{r}_{xy0}+\boldsymbol{z}_0$ holds, where $\boldsymbol{z}_0=(0,0,z_0)^{\mathrm{T}}$ is the part along the z-axis and $\boldsymbol{r}_{xy0}=(r_{x0},r_{y0},0)^{\mathrm{T}}$ is the part in the plane xOy. $\overrightarrow{OP}$ in the reference coordinate system is $\hat{\boldsymbol{r}}_0=(r_{X0},r_{Y0},r_{Z0})^{\mathrm{T}}$. After time t, the point O moves to O', the reference coordinate system (X,Y,Z) translates from the O to O', and the local coordinate system changes from (x,y,z) to (x',y',z'). The point P moves to P'. The coordinate $\overrightarrow{O'P'}$ is $\boldsymbol{r}=(r_{x0},r_{y0},z_0)^{\mathrm{T}}$ in (x',y',z') and $\hat{\boldsymbol{r}}=(r_X,r_Y,r_Z)^{\mathrm{T}}=\mathscr{R}_{\text{init}}\boldsymbol{r}$ in (X,Y,Z). The rotation of point P is expressed as

$$\mathscr{R}_{\text{rotating}}=\exp(\Omega\hat{\omega}'t)=\mathbf{I}+\hat{\omega}'\sin(\Omega t)+\hat{\omega}'^2[1-\cos(\Omega t)], \quad (1)$$

where $\hat{\omega}'=\begin{bmatrix} 0 & -\omega_Z' & \omega_Y' \\ \omega_Z' & 0 & -\omega_X' \\ -\omega_Y' & \omega_X' & 0 \end{bmatrix}$, $\Omega=\|\hat{\boldsymbol{\omega}}\|=\|\boldsymbol{\omega}\|$ and

$\bar{\boldsymbol{\omega}}'=\hat{\boldsymbol{\omega}}/\Omega=(\omega_X',\omega_Y',\omega_Z')^{\mathrm{T}}$. So the coordinate of point P' in the global coordinate system (U,V,W) is expressed as

$$\overrightarrow{QP'}=\overrightarrow{QO}+\overrightarrow{OO'}+\overrightarrow{O'P'}=\boldsymbol{R}_0+\boldsymbol{v}t+\mathscr{R}_{\text{rotating}}\hat{\boldsymbol{r}}_0, \quad (2)$$

and the corresponding distance is

$$\begin{aligned} r(t) &= \left\|\boldsymbol{R}_0+\boldsymbol{v}t+\mathscr{R}_{\text{rotating}}\hat{\boldsymbol{r}}_0\right\| \\ &= \sqrt{(\boldsymbol{R}_0+\boldsymbol{v}t+\mathscr{R}_{\text{rotating}}\hat{\boldsymbol{r}}_0)^{\mathrm{T}}(\boldsymbol{R}_0+\boldsymbol{v}t+\mathscr{R}_{\text{rotating}}\hat{\boldsymbol{r}}_0)} \end{aligned}, \quad (3)$$

B. Transmitting signal

The radar transmitting signal consists of M orthogonal coding signal, and the mth orthogonal coding signal can be written as

$$p_m(t_k)=\text{rect}\left(\frac{t_k-mT_I}{T_p}\right)\mathrm{C}_m\left(t_k-mT_I\right)\exp\left(\mathrm{j}2\pi f_c t_k\right), \quad (4)$$

where t_k is the fast time, $\text{rect}(\cdot)$ is the rectangular window, f_c is the carrier frequency, T_I is the time delay between the two orthogonal coding signals, $T_p=MT_I$ is the code length duration, and $\mathrm{C}_m\left(t_k-mT_I\right)$ is the mth orthogonal Gold code with the time delay mT_I.

The Gold sequence $\mathrm{C}_m\left(t_k\right)$ holds

$$\int \mathrm{C}_i\left(t_k\right)\mathrm{C}_j^{\mathrm{H}}\left(t_k\right)dt_k=\begin{cases} 1, & i=j \\ 0, & i\neq j \end{cases}, \quad (5)$$

and the filter matching result is

$$R_G(\tau)\approx\begin{cases} \dfrac{T_p}{T_b}\left(1-\dfrac{|\tau|}{T_b}\right), & |\tau|\le T_b \\ 0, & |\tau|>T_b \end{cases}. \quad (6)$$

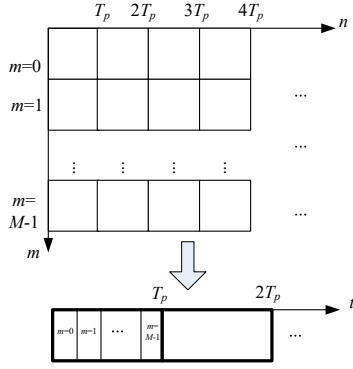where τ is the time delay, T_b is the code width. So it is the

Fig. 2. The rearrangement of the virtual pulses.

Fig. 3. The geometry for solving the range profile of the spinning target.

triangle function with the width $2T_b$. The pulse width changes from T_p to T_b, and the amplitude is T_p/T_b times, which means that the Gold sequence can realize the pulse compression and achieve the high range resolution profile of targets [10]. Besides, the Gold sequence with a longer code length has lower sidelobes and better imaging performance. For convenience in analyzing, $R_G(\tau)$ can be approximated to $T_p/T_b \text{rect}(\tau/T_b)$ since it is a pulse signal with a high peak value.

The overlapped transmitting signals can be expressed as

$$p(t_k) = \sum_{m=1}^{M} \text{rect}\left(\frac{t_k - mT_I}{T_p}\right) C_m(t_k - mT_I)\exp(j2\pi f_c t_k), \quad (7)$$

For any scatterer P on the target, the echo signal can be expressed as

$$s_0(t_k) = \sigma_0 \sum_{m=1}^{M} \text{rect}\left(\frac{t_k - mT_I - \tau}{T_p}\right) \\ C_m(t_k - mT_I - \tau)\exp(j2\pi f_c(t_k - \tau)) \quad , \quad (8)$$

where σ_0 is the scattering intensity, τ is the time delay caused by the distance from the radar to the scatterer. The matched filtering result of the echo signal and the M orthogonal coding signal can be expressed as

$$s_n(t_k, m) = \sigma_0 \frac{T_p}{T_b}\text{rect}((t_k - \tau)/T_b)\exp\left(j\frac{4\pi}{c}f_c(t - \tau)\right), \quad (9)$$

The baseband signal of (9) can be achieved by down-conversion and it can be expressed as

$$s_d(t_k, m) = \sigma_0 \frac{T_p}{T_b}\text{rect}((t_k - \tau)/T_b)\exp\left(j\frac{4\pi}{c}f_c \tau\right), (10)$$

Since the mth orthogonal coding signal is with time delay mT_I, (10) can be regarded as a virtual pulse transmitted by an equivalent antenna. After the rearrangement of the virtual pulses, the full time of the radar transmitted signal can be expressed as

$$t = nT_p + mT_I + t_k,, \quad (11)$$

where $n = 0,1,\cdots N-1, m = 0,1,\cdots M-1$, and N is the pulse number. Then the equivalent slow time is $t_m = nT_p + mT_I$, which is shown in Fig. 2.

C. 2D imaging for spinning space target

Suppose the target translation can be accurately compensated, and the mth orthogonal coding signal in the echo of the target
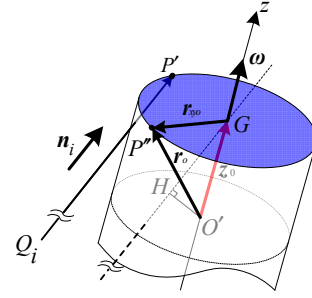
center is chosen as the reference signal. After matched filtering with the rearranged echo signal, the range-slow-time profile can be obtained as

$$s_d(t_k, t_m) = \sigma_0 \frac{T_p}{T_b}\text{rect}\left(\left(t_k - \frac{2}{c}R_\Delta(t_m)\right)/T_b\right), \\ \exp\left(j\frac{4\pi}{c}f_c R_\Delta(t_m)\right) \quad (12)$$

where $R_\Delta(t_m)$ is the distance of $\overrightarrow{O'P'}$ along the line of sight (LOS) direction, and it can be expressed as

$$R_\Delta(t_m) = r(t_m) - R_{ref}(t_m), \quad (13)$$

where $R_{ref}(t_m)$ is the reference range, and $r(t_m)$ is the range from the scatterer P' to the radar at slow time t_m. In the range-slow-time plane, the peak position of the range profile is changed with $R_\Delta(t_m)$. The peak curve reflects the motion characteristics of the spinning target. According to the far-field approximation, (13) can be expressed as

$$R_\Delta(t_m) \approx \overrightarrow{O'P'} \cdot \boldsymbol{n} = \left(\boldsymbol{\mathfrak{R}}_{\text{rotating}}(t_m)\vec{r}_0\right)^T \boldsymbol{n}, \quad (14)$$

where $\boldsymbol{n}$ is the unit vector of the LOS direction $\overrightarrow{QP'}$.

As shown in Fig. 3, $r(t_m)$ is the range of $\overrightarrow{QP'}$, $R_{ref}(t_m)$ is the range of $\overrightarrow{QO'}$, point G is the rotation center of the scatterer P'', $\boldsymbol{r}_{xy0}$ is the vector in the rotation plane of P'', $\overline{HG}$ is parallel to $\overrightarrow{QP'}$, $\boldsymbol{r}_0$ is the vector of $\overrightarrow{O'P''}$. In the local coordinate system, the part of $\boldsymbol{r}_0$ along the z-axis is $\boldsymbol{z}_0$, and the projection of $\boldsymbol{z}_0$ along the LOS direction is $\overline{HG}$. Then (14) can be further expressed as

$$R_\Delta(t_m) = \left\|\overline{HG}\right\| + \boldsymbol{r}_{xy0}^T \boldsymbol{n} \\ = \left\|\overline{HG}\right\| + \left\|\boldsymbol{r}_{xy0}\right\|\cos(\Omega t_m + \psi)\sin\varepsilon \quad (15)$$

where ψ is the angle between the plane GHO' and $\boldsymbol{r}_{xy0}$ at $t_m=0$, Ω is the spinning angular frequency, ε is the angle between $\boldsymbol{n}$ and the angular velocity vector $\boldsymbol{\omega}$.

The spinning radius of the scatterer P'' is denoted by $r = \|\boldsymbol{r}_{xy0}\|$. Since $\|\overline{HG}\| = \boldsymbol{z}_0 \cdot \boldsymbol{n}_i = z_0\cos\varepsilon_i$ holds, (15) can be further expressed as

$$R_\Delta(t_m) = z_0\cos\varepsilon + r\cos(\Omega t_m + \psi)\sin\varepsilon \\ = z_0\cos\varepsilon + (r\cos(\psi)\cos(\Omega t_m) - r\sin(\psi)\sin(\Omega t_m))\sin\varepsilon \quad ,(16)$$
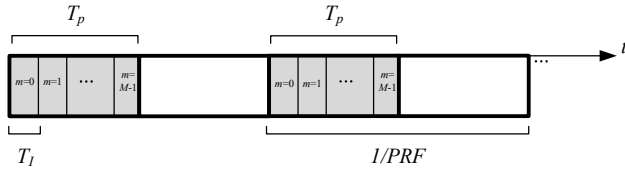
Fig. 4. The virtual pulses are blocked sparse.

Fig. 5. The geometry of the imaging plane.

Let $x_0 = r\cos(\psi)$ and $y_0 = r\sin(\psi)$, then the coordinate of P is (x_0, y_0, z_0). In the small-angle approximation, (16) can be further expressed as

$$R_\Delta(t_m) = z_0 \cos\varepsilon + \left(x_0 \cos(\Omega t_m) - y_0 \sin(\Omega t_m)\right)\sin\varepsilon \\ \approx z_0 \cos\varepsilon + \left(x_0 - y_0\Omega t_m\right)\sin\varepsilon, \quad (17)$$

Then the range-slow-time profile in (12) can be further expressed as

$$s_d(t_k, t_m) = \sigma_0 \frac{T_p}{T_b} \text{rect}\left(\left(t_k - \frac{2}{c}\left(z_0\cos\varepsilon + (x_0 - y_0\Omega t_m)\sin\varepsilon\right)\right)/T_b\right) \\ \exp\left(\text{j}\frac{4\pi}{c}f_c\left(z_0\cos\varepsilon + x_0\sin\varepsilon\right)\right)\exp\left(\text{j}\frac{4\pi}{c}f_c\left(-y_0\Omega t_m\sin\varepsilon\right)\right). \quad (18)$$

The first term in (18) is a narrow pulse with width T_b like the impulse signal. At different slow time t_m, the change of the range peak compared with

$$\text{rect}\left(\left(t_k - \frac{2}{c}\left(z_0\cos\varepsilon + x_0\sin\varepsilon\right)\right)/T_b\right), \quad (19)$$

is proportional to

$$\frac{2}{c}\left(-y_0\Omega t_m\sin\varepsilon\right), \quad (20)$$

The third term in (18) causes the phase change of range profile, and the change is proportional to

$$\frac{2}{c}f_c\left(-y_0\Omega t_m\sin\varepsilon\right), \quad (21)$$

When the carrier frequency is in Ku-band, (21) is 10^8-10^{10} times as much as (20). In addition, Ωt_m is usually a small angle to avoid the azimuth ambiguity. So (18) can be expressed as

$$s_d(t_k, t_m) \approx \sigma_0 \frac{T_p}{T_b} \text{rect}\left(\left(t_k - \frac{2}{c}\left(z_0\cos\varepsilon + x_0\sin\varepsilon\right)\right)/T_b\right) \\ \exp\left(\text{j}\frac{4\pi}{c}f_c\left(z_0\cos\varepsilon + x_0\sin\varepsilon\right)\right)\exp\left(\text{j}\frac{4\pi}{c}f_c\left(-y_0\Omega t_m\sin\varepsilon\right)\right). \quad (22)$$

With the assumption that the virtual pulses are uniformly distributed, azimuth compression can be realized by Fourier transformation to the slow-time t_m, and the result is

$$S_d(t_k, f_m) = \sigma_0 \frac{T_p}{T_b} \text{rect}\left(\left(t_k - \frac{2}{c}\left(z_0\cos\varepsilon + x_0\sin\varepsilon\right)\right)/T_b\right) \\ \text{sinc}\left(B_m\left(f_m + y_0\sin\varepsilon\right)\right)\exp\left(\text{j}\frac{4\pi}{c}f_c\left(z_0\cos\varepsilon + x_0\sin\varepsilon\right)\right), \quad (23)$$

where $\text{sinc}(\cdot)$ denotes the sinc function and the bandwidth is

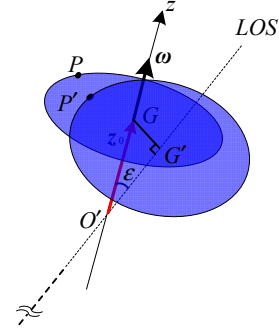$$B_m = c/\left(2f_c\Omega t_m\right)\big|_{t_m = \max(t_m)}.$$

III. AZIMUTH COMPRESSION FOR SPARSE VIRTUAL PULSES

The imaging method in the above section assumes that the virtual pulses are uniformly distributed. For the monostatic pulse radar, however, the transmitting duration and receiving duration should avoid overlapping. As shown in Fig. 4. The gray parts are the transmitting duration and the white parts are the receiving duration. As a result, the virtual pulses are incomplete in full time, where PRF is the real pulse repetition frequency. The missed virtual pulse number in a real pulse duration is $N_p = \lceil 1/(PRF \cdot T_I)\rceil - M$, where $\lceil \cdot \rceil$ is the rounding operator. For all N real pulses, the complete virtual pulse number is $N\lceil 1/(PRF \cdot T_I)\rceil$.

The peak coordinate of (23) is $(z_0\cos\varepsilon + x_0\sin\varepsilon, -y_0\sin\varepsilon)$, which is the projection coordinate of the scatterer P on the imaging plane. As shown in Fig. 5, G' is the closest point on the LOS to the rotation center G, and the imaging plane through the LOS direction is perpendicular to the line GG'.

The observation area is divided by $N_r \times N_a$ grids on the imaging plane, where N_r is the grid number in the LOS direction and N_a is the grid number in the cross-LOS direction. Then the scattering coefficients of the observation area can be expressed as

$$\mathbf{\Xi} = \begin{bmatrix} \sigma_{1,1} & \cdots & \sigma_{1,N_r} \\ \vdots & \ddots & \vdots \\ \sigma_{N_a,1} & \cdots & \sigma_{N_a,N_r} \end{bmatrix}, \quad (24)$$

Then the discrete form of the formula (22) in the spatial domain can be expressed as

$$s_d(t_k, t_m) = \sum_{i=1}^{N_r}\sum_{j=1}^{N_a} \sigma_{j,i} \frac{T_p}{T_b}\text{rect}\left(\left(t_k - \frac{2}{c}\left(x'(i)\right)\right)/T_b\right) \\ \exp\left(\text{j}\frac{4\pi}{c}f_c\left(x'(i)\right)\right)\exp\left(\text{j}\frac{4\pi}{c}f_c\left(-y'(j)\Omega t_m\right)\right). \quad (25)$$

where $x'(i)$ denotes the i-th grid in the LOS direction and $-y'(j)$ denotes the j-th grid in the cross-LOS direction. Since the super-resolution imaging is not covered by this paper, the grid number along the range direction N_r is equal to the range sampling number, and the grid number along the cross-range direction N_a is equal to the complete virtual pulse number $N/(PRF \cdot T_I)$.

For the complete signal, after range compression and

normalization, it can be expressed as $\mathbf{S}=[\boldsymbol{s}_1,\boldsymbol{s}_2,...,\boldsymbol{s}_{N_r}]\in\mathbb{C}^{N_a\times N_r}$, where $\boldsymbol{s}_i=[s_{1,i},s_{2,i},...,s_{N_a,i}]^{\mathrm{T}}\in\mathbb{C}^{N_a\times1}$ and $^{\mathrm{T}}$ is the transposition operator. Since $\boldsymbol{s}_i$ denotes the signal after range compression at $t_{k,i}$, where $t_{k,i}=\frac{2}{c}(x'(i))$ is the i-th discrete fast-time cell, the element of $\boldsymbol{s}_i$ can be expressed as

$$s_{j,i}=\boldsymbol{\varphi}_i\boldsymbol{\sigma}, \tag{26}$$

where $\boldsymbol{\sigma}=[\sigma_{1,i},\sigma_{1,i},...,\sigma_{N_a,i}]^{\mathrm{T}}$, $\boldsymbol{\varphi}_i=[\varphi_{1,i},\varphi_{1,i},...,\varphi_{N_a,i}]$, and

$$\varphi_{j,i}=\exp\left(\mathrm{j}\frac{4\pi}{c}f_c\left(x'(i)\right)\right)\exp\left(\mathrm{j}\frac{4\pi}{c}f_c\left(-y'(j)\Omega t_{m,j}\right)\right). \tag{27}$$

As shown in Fig. 4, the real signal is block-missing in the slow-time domain since the virtual pulses are incomplete. The block-missed signal is denoted by $\mathbf{S}'=[\boldsymbol{s}_1',\boldsymbol{s}_2',...,\boldsymbol{s}_{N_r}']\in\mathbb{C}^{N_a'\times N_r}$, where $\boldsymbol{s}_i'\in\mathbb{C}^{N_a'\times1}$ and it can be expressed as

$$\boldsymbol{s}_i'=\boldsymbol{\Phi}\boldsymbol{s}_i=\boldsymbol{\Phi}\boldsymbol{\Psi}_i\boldsymbol{\sigma}, \tag{28}$$

where $\boldsymbol{\Psi}_i=[\boldsymbol{\varphi}_1^{\mathrm{T}},\boldsymbol{\varphi}_2^{\mathrm{T}},...,\boldsymbol{\varphi}_{N_a}^{\mathrm{T}}]^{\mathrm{T}}\in\mathbb{C}^{N_a\times N_a}$ is the sparse basis matrix, and $\boldsymbol{\Phi}\in\mathbb{C}^{N_a'\times N_a}$ is the measurement matrix. If the signal is complete, the measurement matrix is a unit matrix. According to the signal missing form shown in Fig. 4, the measurement matrix $\boldsymbol{\Phi}$ is a part of the unit matrix, which can be expressed as

$$\boldsymbol{\Phi}=\begin{bmatrix} \boldsymbol{I}_{M\times M} & & & & & \\ & \boldsymbol{0}_{M\times N_p} & \boldsymbol{I}_{M\times M} & & & \\ & & & \boldsymbol{0}_{M\times N_p} & & \\ & & & & ... & \\ & & & & & \boldsymbol{I}_{M\times M} \\ & & & & & \boldsymbol{0}_{M\times N_p} \end{bmatrix}, \text{ where}$$

$\boldsymbol{I}_{M\times M}$ is the M-by-M unit matrix, and $\boldsymbol{0}_{M\times N_p}$ is the M-by-N_p zero matrix. We transform (28) from a complex model to a real model as

$$\boldsymbol{y}_i=\mathbf{A}_i\boldsymbol{x}_i \tag{29}$$

where $\boldsymbol{y}_i=\begin{bmatrix}\mathrm{Re}(\boldsymbol{s}_i')\\\mathrm{Im}(\boldsymbol{s}_i')\end{bmatrix},\mathbf{A}_i=\begin{bmatrix}\mathrm{Re}(\boldsymbol{\Psi}_i) & -\mathrm{Im}(\boldsymbol{\Psi}_i)\\\mathrm{Im}(\boldsymbol{\Psi}_i) & \mathrm{Re}(\boldsymbol{\Psi}_i)\end{bmatrix},\boldsymbol{x}_i=\begin{bmatrix}\mathrm{Re}(\boldsymbol{x}_i)\\\mathrm{Im}(\boldsymbol{x}_i)\end{bmatrix}$,

$\mathrm{Re}(\cdot)$ and $\mathrm{Im}(\cdot)$ denote the real part and the imaginary part, respectively.

Due to the sparsity distribution of scattering centers on the aerospace targets, $\boldsymbol{x}_i$ is a sparse vector, which can be obtained from (29) by solving the following optimization:

$$\boldsymbol{x}_i=\arg\min\|\boldsymbol{x}_i\|_0, \quad \text{s.t.} \quad \boldsymbol{y}_i=\mathbf{A}_i\boldsymbol{x}_i, \tag{30}$$

where $\|\cdot\|_0$ is the 0-norm operator. (30) is a classical sparse signal recovery problem, and it can be solved by the Smoothed L0-norm (SL0) algorithm. Here is a brief introduction to the SL0 algorithm and the detailed procedure is shown in [22]. To approximate the 0-norm, which is a discontinuous function, the SL0 algorithm utilizes a continuous Gaussian function $f_\lambda(\boldsymbol{x}_i)=\exp(-\boldsymbol{x}_i^2/2\lambda^2)$. The relation between the $\|\boldsymbol{x}_i\|_0$ and $f_\lambda(\boldsymbol{x}_i)$ is

---

Algorithm 1: Modified SL0 algorithm for azimuth compression

Input: The signal after range compression $\mathbf{S}'$; measurement matrix $\boldsymbol{\Phi}$; spare basis matrix $\boldsymbol{\Psi}$;
Output: Scattering coefficient matrix $\boldsymbol{\Xi}$;
Initialization: $\mathbf{A}^+=\mathbf{A}^{\mathrm{T}}(\mathbf{A}\mathbf{A}^{\mathrm{T}})^{-1}$, $\mathbf{X}_0=\mathbf{A}^+\mathbf{Y}$, inner loop times L
Set a sequence as $\{\lambda_0,\lambda_1,...,\lambda_j,...\},\lambda_j=c_0\lambda_{j-1}$, where $c_0\in(0,1)$ is a constant, λ_0 is the max element in $\mathbf{X}_0$. Step size μ of the gradient descent. Threshold η.
Let $j=0$
While $\|\mathbf{Y}-\mathbf{AX}\|_2>\eta$ **do**
   Let $\lambda=\lambda_j$ and $\mathbf{X}=\mathbf{X}_j$
     For $l\in[1,L]$ **do**
     Gradient calculation: $\nabla F_\lambda(\mathbf{X})=\mathbf{X}\odot\exp\left(-\mathbf{X}^2/2\lambda^2\right)$;
     Steepest descent: $\mathbf{X}=\mathbf{X}-\mu\times\nabla F_\lambda(\mathbf{X})$;
     Feasible region projection: $\mathbf{X}=\mathbf{X}-\mathbf{A}^+\left(\mathbf{AX}'-\mathbf{Y}\right)$;
     end for
   Set $j=j+1,\mathbf{X}_j=\mathbf{X}$.
end while
$\boldsymbol{\Xi}=\mathbf{X}(1:N_a,:)+\mathrm{j}\mathbf{X}(N_a+1:2N_a,:)$

$$\lim_{\lambda\to0}F_\lambda(\boldsymbol{x}_i)=\lim_{\lambda\to0}\sum_{i=1}^{N_a}f_\lambda(\boldsymbol{x}_i(i))=N_a-\|\boldsymbol{x}_i\|_0, \tag{31}$$

When λ is small enough, the maximization of $F_\lambda(\boldsymbol{x}_i)$ is equal to the minimization of the $\|\boldsymbol{x}_i\|_0$. A decreasing sequence of λ is utilized to obtain the global maximum of $F_\lambda(\boldsymbol{x}_i)$ instead of the local maxima and the steepest ascent method is used to maximize $F_\lambda(\boldsymbol{x}_i)$ for each λ.

However, if the azimuth compression is realized by solving (30), the SL0 algorithm should run N_r times because $\boldsymbol{s}_i'$ is only the one row in the signal matrix $\mathbf{S}'$. To realize the azimuth compression by running the SL0 algorithm, the difference between the sparse basis matrixes of the rows in $\mathbf{S}'$ should be eliminated at first. According to (27), the difference between different basis matrixes is caused by the phase term $\exp\left(\mathrm{j}4\pi f_c\left(x'(i)\right)/c\right)$. Since $x'(i)$ is the i-th grid along the range direction, it is known after dividing the observation area and can be directly compensated from $\boldsymbol{s}_i'$. After this phase compensation, (28) can be expressed as

$$\boldsymbol{s}_i''=\boldsymbol{\Phi}\boldsymbol{\Psi}\boldsymbol{\sigma}, \tag{32}$$

where $\boldsymbol{s}_i''=\boldsymbol{s}_i'\cdot\exp\left(-\mathrm{j}4\pi f_c\left(x'(i)\right)/c\right)$ is the signal after phase compensation and $\boldsymbol{\Psi}=\boldsymbol{\Psi}_i\cdot\exp\left(-\mathrm{j}4\pi f_c\left(x'(i)\right)/c\right)$ is the same sparse basis matrix for $\boldsymbol{s}_i'',i=1,2,...,N_r$. As a result, the signal matrix $\mathbf{S}'$ after phase compensation for each row can be expressed as

$$\mathbf{S}''=\boldsymbol{\Phi}\mathbf{S}=\boldsymbol{\Phi}\boldsymbol{\Psi}\boldsymbol{\Xi}, \tag{33}$$

Like (29), (33) is transformed to a real model as

$$\mathbf{Y}=\mathbf{AX} \tag{34}$$

where $\mathbf{Y}=\begin{bmatrix}\mathrm{Re}(\mathbf{S}_i'')\\\mathrm{Im}(\mathbf{S}'')\end{bmatrix},\mathbf{A}=\begin{bmatrix}\mathrm{Re}(\boldsymbol{\Phi}\boldsymbol{\Psi}) & -\mathrm{Im}(\boldsymbol{\Phi}\boldsymbol{\Psi})\\\mathrm{Im}(\boldsymbol{\Phi}\boldsymbol{\Psi}) & \mathrm{Re}(\boldsymbol{\Phi}\boldsymbol{\Psi})\end{bmatrix},\mathbf{X}=\begin{bmatrix}\mathrm{Re}(\boldsymbol{\Xi})\\\mathrm{Im}(\boldsymbol{\Xi})\end{bmatrix}$.
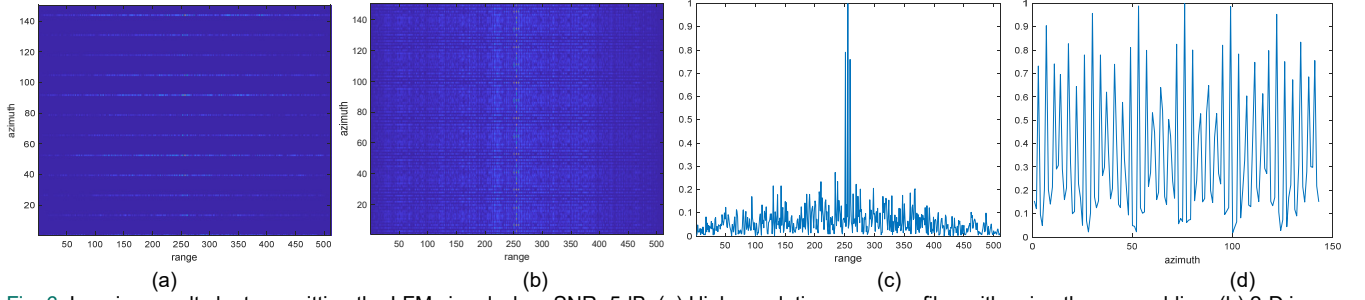
Fig. 6. Imaging results by transmitting the LFM signal when SNR=5dB. (a) High-resolution range profiles with azimuth zero-padding; (b) 2-D image; (c) Range profile of the 76th row in (b); (d) Azimuth profile of the 255th column in (b);
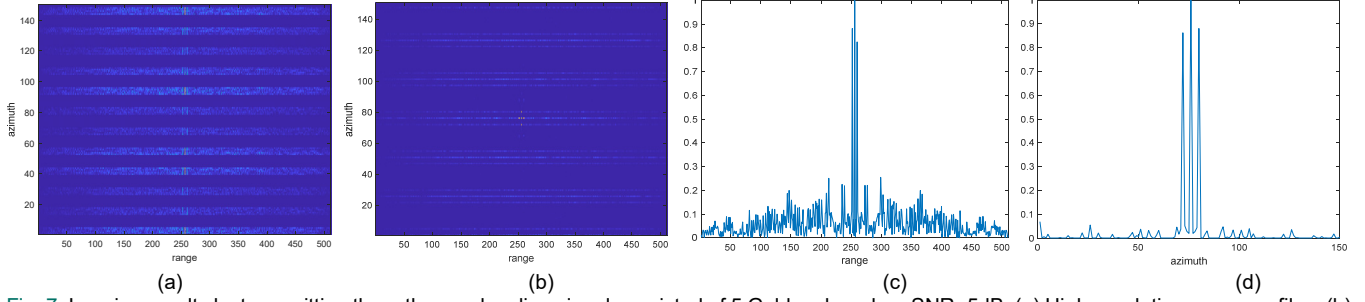

Fig. 7. Imaging results by transmitting the orthogonal coding signal consisted of 5 Gold codes when SNR=5dB. (a) High-resolution range profiles; (b) 2-D image; (c) Range profile of the 76th row in (b); (d) Azimuth profile of the 255th column in (b);

Then the corresponding optimization problem is

$$\mathbf{X} = \arg\min \|\mathbf{X}\|_0, \quad \text{s.t.} \quad \mathbf{Y} = \mathbf{AX}, \quad (35)$$

For $\mathbf{x}_i$, a decreasing sequence $\{\lambda_0, \lambda_1, ...,\}$ is utilized in the SL0 algorithm, and λ_0 should be large enough to avoid the local maximum of $F_\lambda(\mathbf{x}_i)$. To modify the SL0 algorithm for(35), the λ_0 should be large enough for each column of $\mathbf{X}$, and we set λ_0 as the max element in $\mathbf{X}_0$, where $\mathbf{X}_0 = \mathbf{A}^T(\mathbf{AA}^T)^{-1}\mathbf{Y}$ is the initial value of $\mathbf{X}$. For each λ in the decreasing sequence $\{\lambda_0, \lambda_1, ...,\}$, the steepest ascent method to maximize $F_\lambda(\mathbf{X})$ is divided into three steps: gradient calculation, steepest descent, and feasible region projection, which can be expressed as

$$\nabla F_\lambda(\mathbf{X}) = \mathbf{X} \odot \exp(-\mathbf{X}^2/2\lambda^2)$$
$$\mathbf{X} = \mathbf{X} - \mu \times \nabla F_\lambda(\mathbf{X}) \quad\quad (36)$$
$$\mathbf{X} = \mathbf{X} - \mathbf{A}^+(\mathbf{AX}' - \mathbf{Y})$$

where ∇ is the gradient operator, $\odot$ is the dot product, μ is the step size, and $\mathbf{A}^+ = \mathbf{A}^T(\mathbf{AA}^T)^{-1}$ is the pseudo inverse of $\mathbf{A}$. The modified SL0 algorithm for azimuth compression is described in Algorithm 1.

IV. EXPERIMENTS

In this section, both simulations and experiments are carried out to verify the proposed imaging method.

A. Simulations

In Inverse Synthetic Aperture Radar (ISAR) imaging, the imaging angle θ and the azimuth resolution ρ_a hold the relation $\rho_a = \lambda/2\theta$, where λ is the wavelength. As a result, the azimuth resolution can be improved by increasing the imaging angle. However, since the approximation $\sin\theta \approx \theta$ is used in the turntable model, the increase of the imaging angle cannot be unlimited. Generally, the spinning frequency of the space targets is no more than 10Hz. As a result, the imaging angle is 14.4°, the spinning frequency of the target is 5Hz and the PRF is 1500 Hz in the simulation. Since the imaging angle is caused by the spinning motion of the target, only 12 pulses can be received. For contrast, the Linear Frequency Modulation (LFM) signal and the orthogonal Gold coding signal are utilized as the transmitted signal. For the transmitted LFM signal, the carrier frequency is 15GHz, the bandwidth is 6GHz and the pulse duration is 4e-5s. The pulse duration of 4e-5s is the default value in the Signal Generator. The range resolution is $\rho_r = c/2B = 0.025$m and the azimuth resolution is $\rho_a = \lambda/2\theta = 0.02\text{m}/(2 \cdot 14.4° \cdot \pi/180°) \approx 0.04\text{m}$. Because the azimuth resolution can also be expressed as $\rho_a = c/(2\theta \cdot f_c)$, the azimuth resolution changes with the carrier frequency. For the orthogonal coding signal, the carrier frequency is also 15GHz, the number of the Gold codes is 5, the Gold code width T_b is 1.5e-9s, the Gold code length is 255, the time delay T_I is 3.7e-08s. To simulate the environmental noise in the real case, the white Gaussian noise is added to the received signal and the signal-noise ratio (SNR) is 5dB.

Fig. 6 shows the imaging results by transmitting the LFM signal. Only 12 effective high-resolution range profiles (HRRP) can be obtained after range compression for the 12 received pulses. For contrast, the 12 effective HRRPs are zero-padded along the azimuth direction to form the 144 HRRPs, which are shown in Fig. 6(a). Fig. 6(b) shows the 2-D image after azimuth compression. Fig. 6(c) and Fig. 6(d) show the range profile of the 76th row and the azimuth profile of the 255th column, respectively.

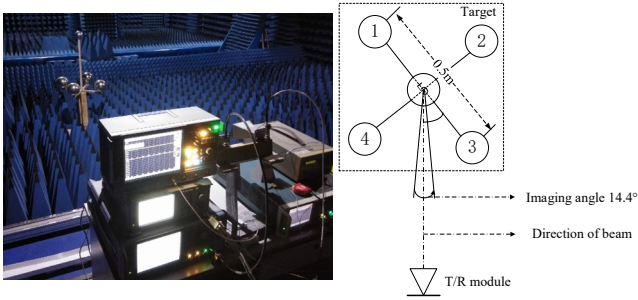To verify the proposed imaging method, the orthogonal

Fig. 8. Optical picture and the top-view diagram of the experiment system;

coding signal consisted of 5 Gold codes are designed and transmitted to the target, and then the one-dimensional range profile sequence of the target for the single Gold coded signal can be obtained after orthogonal signal separation by matching filtering. Fig. 7 shows the imaging results by transmitting the orthogonal coding signal consisted of 5 Gold codes, which are randomly generated by MATLAB. After orthogonal signal separation and range compression, 60 effective HRRPs can be obtained. The 60 effective HRRPs are block- sparse distributed along the azimuth direction, which is shown in Fig. 7(a). Fig. 7(b) shows the 2-D image obtained after azimuth sparse compression by the modified SL0 algorithm. Fig. 7(c) and Fig. 7(d) show the range profile of the 76th row and the azimuth profile of the 255th column, respectively.

Compared with Fig. 6(a) and Fig.7(a), 60 effective HRRPs can be obtained by transmitting the orthogonal coding signal but only 12 effective HRRPs can be obtained by transmitting the LFM signal. In Fig. 6(b), serious azimuth ambiguity occurs because the effective pulses are multiplied after orthogonal signal separation and the azimuth sparse compression is effective. However, in Fig. 7(b), the azimuth ambiguity disappears because the effective pulses in this case are enough for sparse reconstruction in azimuth compression. This issue can also be seen from the azimuth profile in Fig. 6(d) and Fig. 7(d). Moreover, the sidelobe of the range profile decreases significantly by comparing Fig. 6(c) and Fig.7(c).

B. Experiments

To validate the proposed method further, the principal prototype experiment has been performed. The target and the diagram of the experimental system are shown in Fig. 8. The target is constituted of five metal balls and it can rotate around the vertical axis. The parameters in the experiments are the same as those in the simulations.

In this experiment, the conventional ISAR imaging method and the proposed method are compared in the condition of short-time observation. The experiment results of the conventional method are shown in Fig. 9. Fig. 9(a) and Fig. 9(c) show the zero-padded HRRPs and the linear interpolated HRRPs, respectively. Fig. 9(b) and Fig. 9(d) shows the azimuth matched filtering results of Fig. 9(a) and Fig. 9(c). The experiment results of the proposed method with the code length 127, 255, 511, 1023, and 2047 are shown in Fig. 10 from top to bottom. Fig. 10(a) and shows the zero-padded HRRPs. Fig. 10(b) shows the 2-D image after azimuth sparse compression by the modified SL0 algorithm. Moreover, the inverse Fourier
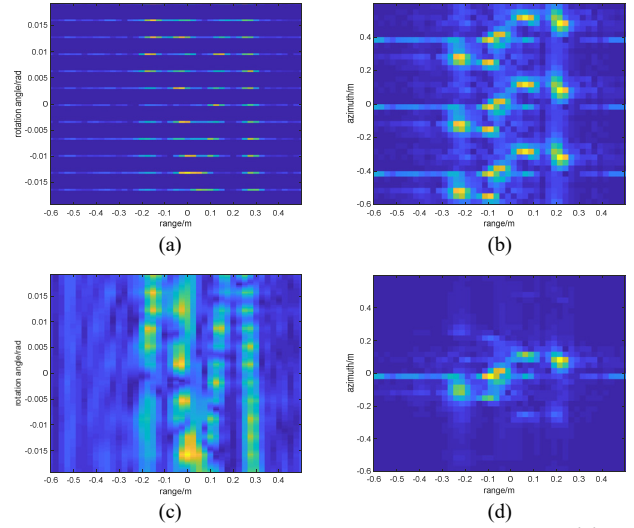

Fig. 9. Experiment results by transmitting the LFM signal. (a) Zeros padded high-resolution range profiles; (b) Azimuth compression of (a); (c) Interpolated high-resolution range profiles; (d) Azimuth compression of (c).
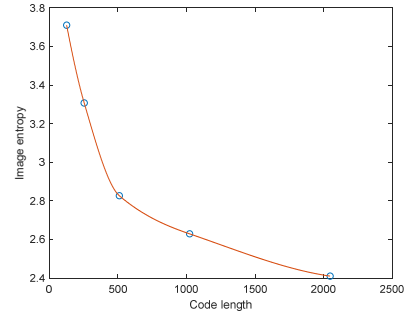

Fig. 11. Variation of the image entropy with the code length.

transform results of Fig. 10(b) in the azimuth direction are shown in Fig. 10(c), from which we can see the block-sparse distributed HRRPs are well-recovered.

To declare the improvement of the proposed method compared with the conventional method, Fig. 9(b), Fig. 9(d), and Fig.10(b) should be compared. It can be seen that serious azimuth ambiguity occurs in Fig. 9(b) and the imaging distortion occurs in Fig. 9(d), which means that the conventional imaging method fails to image the target. On the contrary, the azimuth ambiguity and imaging distortion disappear in Fig. 10(b) which means that the proposed method is effective. The reason is as follows: In this experiment, the observation time is $14.4°/360°/5\text{Hz}=0.008\text{s}$. Since the proposed method can utilize the target spinning to obtain the azimuth resolution, the well-focused image can be obtained in such a short observation time. However, the conventional imaging method requires observing at least one spinning period 0.2s, so it fails in a short observation time.

To evaluate the imaging quality, the image entropy is calculated as [23]

$$E = -\sum_{m,n} I_{m,n}^2 \log(I_{m,n}^2) \qquad (37)$$

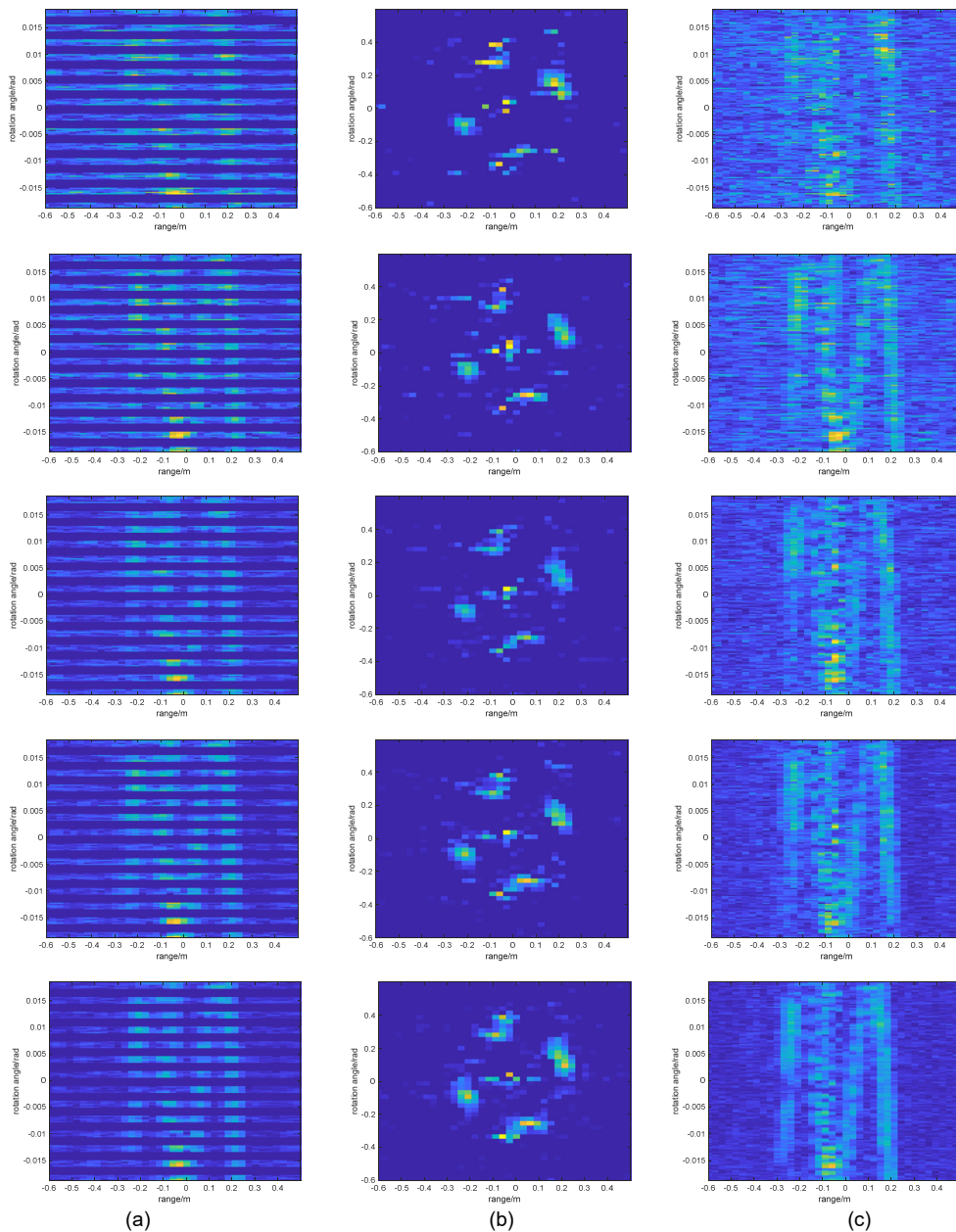where $I_{m,n}$ is the pixel value of the mth row and nth column in

Fig. 10. Experiment results by transmitting the orthogonal coding signal consisted of 5 Gold codes with the code length 127, 255, 511, 1023, and 2047 from top to bottom, respectively. (a) Zeros padded high-resolution range profiles; (b) Azimuth compression by modified SL0; (c) Azimuth Fourier transform results of (b).

the image I. The image entropy can evaluate the focusing property of the image, and a small image entropy corresponds to the image with the good focusing property. The variation curve of the image entropy with the code length is shown in Fig. 11. According to Fig. 11, the image entropy decreases with the increase of code length, which means that the imaging quality of the proposed method is improved with the increase of code length.

V. CONCLUSION

In this paper, we propose a novel sparse imaging method for spinning space targets with short time observation. Compared with the methods requiring the observation for several spinning periods, the observing time of the proposed method only needs

to cover a small percentage of one spinning period. It can reduce the time source of the radar imaging task for a single spinning target. Besides, the more important significance is that imaging with short time observation can be used in multi-target surveillance such as satellites and space debris. The proposed method has potential applications in the utilization and of space resources and space defense.

REFERENCES

[1] E. Pate-Cornell and M. Sachon, "Risks of particle hits during space walks in low Earth orbit," *IEEE Trans. Aerosp. Electron. Syst.*, vol. 37, no. 1, pp. 134–146, Jan. 2001.

[2] R. Min, L. Pereira, T. Paixiao, and et al, "Inscription of Bragg gratings in undoped PMMA mPOF with Nd:YAG laser at 266 nm wavelength," Optics Express, vol. 27, issue. 26, pp. 38039-38048, 2019.

[3] R. Min, C. Marques, Ole. Bang, and B. Ortega, "Moiré phase-shifted fiber Bragg gratings in polymer optical fibers," Optics Fiber Technology, vol. 41, pp. 78-81, March, 2018.

[4] L. Pereira, R. Min, X. Hu, and et al, "Polymer optical fiber Bragg grating inscription with a single Nd:YAG laser pulse," Optics Express, vol. 26, issue. 14, pp. 18096-18104, 2018.

[5] V. C. Chen and M. Martorella, "Inverse Synthetic Aperture Radar Imaging: Principles, Algorithms and Applications," SciTech Publishing, NJ, USA, 2014.

[6] L. Zhang, Z. J. Qiao, M. D. Xing, J. L. Sheng, R. Guo, and Z. Bao, "High-resolution ISAR imaging by exploiting sparse apertures," IEEE Transactions on Antennas & Propagation, vol. 60, no. 2, pp. 997-1008, 2020.

[7] L. Liu, F. Zhou, M. Tao, and Z. Zhang, "A novel method for multi-targets ISAR imaging based on particle swarm optimization and modified clean technique," IEEE Sensors Journal, vol. 16, no. 1, pp. 97-108, 2016.

[8] M. A. Herman and T. Strohmer, "High-resolution radar via compressed sensing," IEEE Transactions on Signal Processing, vol. 57, no. 6, pp. 2275-2284, 2009.

[9] L. Zhang, Z. J. Qiao, M. Xing, Y. Li, and Z. Bao, "High-resolution ISAR imaging with sparse stepped-frequency waveforms," IEEE Transactions on Geoence & Remote Sensing, vol. 49, no. 11, pp. 4630-4651, 2011.

[10] J. Rong, Y. Wang, and T.Han, "Iterative optimization-based ISAR imaging with sparse aperture and its application in interferometric ISAR imaging. IEEE sensors journal, vol. 19, no. 19, pp. 8681-8693, 2019.

[11] Y. Wang, X. Chen, and X. Lu, "ISAR Imaging of the Maneuvering Target with Sparse Aperture Based on the Modified Orthogonal Matching Pursuit," 2019 6th Asia-Pacific Conference on Synthetic Aperture Radar, Nov, Xiamen.

[12] S. J. Son, "Range-Doppler Radar Imaging and Motion Compensation," Artech House, Inc. 2001.

[13] Y. Wang, X. Y. Zhou and R. Z. Zhang, "The Removal of Micro-Doppler Effect in ISAR Imaging Based on Time Recursive Iterative Adaptive

Approach, " IET Radar Sonar & Navigation, vol. 8, 2020. DOI: 10.1049/iet-rsn.2020.0018.

[14] Q. Zhang, Y. Luo and Y. A. Chen, "Micro-Doppler Characteristics of Radar Targets," Elsevier Press, 2016.

[15] H. Li, W. Zhang, Y. Wang and X. Wang, "Method for micro-doppler separation in ISAR imaging based on discrete sinusoidal frequency-modulated transform," Journal of Applied Remote Sensing, vol. 14, no. 3, 2020. DOI: 10.1117/1.JRS.14.036502.

[16] Q. Zhang, T. S. Yeo, H. S. Tan, and Y. Luo, "Imaging of a moving target with rotating parts based on the hough transform," IEEE Transactions on Geoence and Remote Sensing, vol. 46, no. 1, pp. 291–299, Jan. 2008.

[17] X. Bai, F. Zhou, M. Xing, and Z. Bao, "High resolution ISAR imaging of targets with rotating parts," IEEE Transactions on Aerospace & Electronic Systems, vol. 47, no. 4, pp. 2530-2543, Apr. 2011.

[18] X. R. Bai, M. Xing, F. Zhou, G. Lu, and Z. Bao, "Imaging of micromotion targets with rotating parts based on empirical-mode decomposition," IEEE Transactions on Geoence & Remote Sensing, vol. 46, no. 11, pp. 548–556, Nov. 2008.

[19] Y. Wang, X. Huang, and Q. X. Zhang, "Rotation Parameters Estimation and Cross-Range Scaling Research for Range Instantaneous Doppler ISAR Images," IEEE Sensors Journal, vol. 20, no. 3, Mar. 2020. DOI: 10.1109/JSEN.2020.2977665.

[20] Y. Hui and X. R. Bai, "RID image series-based high-resolution three-dimensional imaging of micromotion targets," Journal of Radars, vol. 7, no. 5, pp. 548–556, Oct. 2018.

[21] T. B. Hale, M. A. Temple, B. L. Crossley, "Ambiguity analysis for pulse compression radar using Gold code sequences," Proceedings of the IEEE Radar Conference, Feb, 2001. DOI: 10.1109/NRC.2001.922961.

[22] H. Mohimani, M. Babaie-Zadeh, C. Jutten, "A Fast Approach for Overcomplete Sparse Decomposition Based on Smoothed L-0 Norm," IEEE Transactions on Signal Processing, vol. 57, no. 1, pp. 289-301, Jan. 2009.

[23] L. Xi, L. Guosui, and J. Ni, "Autofocusing of ISAR image based on entropy minimization," IEEE Transactions on Aerospace and Electronic Systems, vol. 35, no. 4, pp. 1240-1252, 1999.